PCCP

Thermal and concentration effects on 1H NMR relaxation of Gd3+ aqua using MD simulations and measurements

Journal:	*Physical Chemistry Chemical Physics*
Manuscript ID	CP-ART-09-2022-004390.R1
Article Type:	Paper
Date Submitted by the Author:	01-Nov-2022
Complete List of Authors:	Pinheiro dos Santos, Thiago J.; Rice University, Chemical and Biomolecular Engineering Valiya Parambathu, Arjun; Rice University, Chemical and Biomolecular Engineering Fraenza, Carla ; Hunter College CUNY, Department of Physics & Astronomy Walsh, Casey; Hunter College CUNY, Department of Physics & Astronomy Greenbaum, Steven; Hunter College CUNY, Department of Physics & Astronomy Chapman, Walter; Rice University, Chemical and Biomolecular Engineering Asthagiri, Dilipkumar; Rice University, Chemical and Biomolecular Engineering Singer, Philip; Rice University, Chemical and Biomolecular Engineering

Journal Name

ARTICLE TYPE

Cite this: DOI: 00.0000/xxxxxxxxxx

Thermal and concentration effects on ^{1}H NMR relaxation of Gd^{3+}–aqua using MD simulations and measurements

Thiago J. Pinheiro dos Santos [a], Arjun Valiya Parambathu [a,b], Carla C. Fraenza [c], Casey Walsh [c], Steve G. Greenbaum [c], Walter G. Chapman [a], Dilip Asthagiri †[a,d], and Philip M. Singer ‡[a]

Received Date
Accepted Date

DOI: 00.0000/xxxxxxxxxx

Gadolinium-based contrast agents are key in clinical MRI for enhancing the longitudinal NMR relativity (r_1) of hydrogen nuclei (^{1}H) in water and improving the contrast among different tissues. The importance of MRI in clinical practice cannot be gainsaid, yet the interpretation of MRI relies on models with severe assumptions, reflecting a poor understanding of the molecular-scale relaxation processes. In a step towards building a clearer understanding of the relaxation processes, here we investigate thermal and concentration effects on r_1 of the Gd^{3+}–aqua complex using both semi-classical molecular dynamics (MD) simulations and measurements. We follow the MD simulation approach recently introduced by [Singer *et al., PCCP*, 2021, **23**, 20974], in which no NMR relaxation model or free-parameter is assumed to predict r_1, thereby bringing new insights into the physics of r_1 on a molecular scale. We expand the autocorrelation function $G(t)$ in terms of molecular modes and determine the thermal activation energies of the two largest modes, both of which are consistent with the range of literature values for rotational diffusion. We also determine the activation energies for translational diffusion and low-field electron-spin relaxation, both of which are consistent with the literature. Furthermore, we validate the MD simulations at human body temperature and concentrations of the paramagnetic ion used in clinical MRI, and we quantify the uncertainties in both simulations and measurements.

1 Introduction

Contrast agents used in Magnetic Resonance Imaging (MRI) are essentially chemical compounds that reduce both T_1 and T_2 of water ^{1}H protons. It is consensus in the literature that gadolinium-based contrast agents (GBCAs) are the most widely used in clinical MRI [1–8]. Because gadolinium(III) (Gd^{3+}) has seven unpaired electrons, its paramagnetic properties considerably reduce the NMR relaxation time of water ^{1}H protons and enhance contrast [9]. The majority of GBCAs are T_1-agents that acts as extracellular fluid agents or blood-pool agents, with different tissue selectivities [1].

For the case of paramagnetic species, the relaxation of nuclear spins through interactions with the unpaired electronic spins from the paramagnetic species play a much stronger role than the nuclear-nuclear relaxation, since the magnetic moment of an unpaired electron is about 658 times larger than the moment of a hydrogen nucleus (^{1}H) [10]. Having this in mind, Solomon [11], Bloembergen, and Morgan [12,13] (SBM) proposed a NMR relaxation model for paramagnetic species inspired by the pioneering work of Bloembergen, Purcell, and Pound (BPP) [14]. Building on Debye's theory of dielectric dispersion, the BPP model associates relaxation with rotational motion of the molecules (hard-spheres) and predicts a mono-exponential decay of the autocorrelation function of the rotational motion. The SBM model in-turn assumes that relaxation depends on a Brownian motion of water molecules around the paramagnetic species, which is called molecular inner-shell. Despite the fact that SBM model is usually employed for modeling NMR relaxation of water ^{1}H around paramagnetic ions within the inner-shell, it is known that such mono-exponential decay models commonly fail to predict NMR relaxation [15–17].

The water ^{1}H far away from the paramagnetic ion encompass the so-called outer-shell, and their relaxation is usually modeled

a, Department of Chemical and Biomolecular Engineering, Rice University, Houston, TX 77005, USA
b, Current address: Department of Chemical and Biomolecular Engineering, University of Delaware, Newark, DE 19716, USA
c, Department of Physics & Astronomy, Hunter College of the City University of New York, New York, NY 10065, USA
d, Oak Ridge National Laboratory, Oak Ridge, TN 37830-6012, USA
†, asthagiridn@ornl.gov
‡, ps41@rice.edu

using the intermolecular relaxation model developed by Hwang and Freed [18] (HF), which improved the classic model by Torrey [19] by taking the structure of the fluid (radial distribution function) into account for modeling translational diffusion while enforcing a force-free hard-sphere boundary condition. Other improvements on the modeling of the outer-shell contribution were made by Ayant and Belorizky [20], as an extension of the original HF model. The so-called Ayant, Belorizky, Hwang and Freed (ABHF) model assumes that the magnetic dipoles are located in the center of hard-spheres diffusing in a viscous continuum. Despite the improvements, this model ignores the anisotropy of the molecules and intermolecular potential interactions (e.g., hydrogen bonds for the case of water) [21].

At the zero-field state (absence of an applied magnetic field), distortions in the paramagnetic coordination environment affects the zero field splitting energies and promotes the so-called electron-spin relaxation. Electron-spin relaxation affects both the inner and outer-shell contributions and has a sizeable contribution at low frequencies $f_0 \leq 5$ MHz [21]. However, at typical frequencies of interest to clinical MRI ($20 \leq f_0 \leq 130$ MHz, or $0.5 \leq B_0 \leq 3$ T equivalently), this effect plays a minor role and is usually assumed to be negligible. We shall refer to the combination of the SBM model for inner-shell, the HF model for outer-shell, and the BPP model for the electron-spin relaxation [22] as the "extended SBM" model.

In this work, we seek to investigate thermal and concentration effects on the NMR relaxation of the $Gd^{3+}-$aqua complex through both semi-classic molecular dynamics (MD) simulations and measurements. Our simulations follow the approach recently introduced by Singer *et al.* (2021) [15], which does not assume any NMR relaxation models or free-parameters to describe the physics of the process. We now validate this MD simulation approach at human body temperature by showing the agreement with measurements. We decompose the relaxation into molecular modes and quantify the temperature dependence in terms of the the activation energies of these modes. Further, we quantify the uncertainties in both simulations and measurements, and we extrapolate the simulation results to different concentrations of the paramagnetic species typically used in clinical MRI.

2 Methodology

2.1 Molecular simulation details

We have investigated the longitudinal NMR relaxation of the $Gd^{3+}-$aqua complex at five different temperatures, namely $T = 5$, 10, 15, 25, and 37°C. Although ligand-field effects are not expected to play a role for $Gd^{3+}-$aqua, electronic density effects are still important for NMR relaxation of the complex because of the large positive charge of the ion. Thus, calculations were performed with the AMOEBA polarizable forcefield for both the water [23] and the ions [24] (also see Supplementary Information). Simulations were performed with the GPU-based OpenMM-7.5.1 [25] package.

We simulate a cubic system under periodic boundary conditions. Following the recommendations for the AMOEBA forcefield [26], the real space electrostatic potential was truncated at 0.9 nm. We employed a cutoff at 1.2 nm for the van der Waals interactions, and a tolerance of 10^{-5} Debye for the mutual convergence of the polarization calculations. Long-range electrostatic interactions were described using the particle-mesh Ewald (PME) method, with a tolerance error of 10^{-5} in the forces. Note that in Ewald's formulation implicitly includes an uniform neutralizing background. This background does not affect the dynamics and also makes feasible simulations with a single cation.

We set up the molecular structures and the simulation box using the Packmol [27] package. All simulation boxes were built with 2006 molecules of water and 1 Gd^{3+} ion. We simulated the systems in the isothermal-isobaric ensemble (NpT) at the desired temperatures and atmospheric pressure (1 atm) using a 1 fs timestep. The equilibration was over 0.2 ns and the production lasted 4 ns. We employed three chains of Nosé-Hoover thermostats with a collision frequency parameter of 10 ps^{-1}, and a Monte Carlo isotropic barostat with a frequency of 50 fs. From these simulations, we calculated the average volume of each system at these conditions after equilibration. The length of the cubic simulation box settles to approximately 40 Å.

We later reassembled the simulation boxes with the corresponding average volume at each given temperature. The new systems were simulated in the canonical ensemble (NVT) with three chains of Nosé-Hoover thermostats at each desired temperature for 2 ns of equilibration and 8 ns of data production. All simulations were performed in triplicate. During the production step, the atomic coordinates were stored every 0.1 ps. The analysis of the data was performed with the last 6.5536 ns (65536 or 2^{16} frames) of the production set.

2.2 Structure and dynamics

The structure of the $Gd^{3+}-$aqua complex at different temperatures was analyzed in terms of the radial distribution function $g_j(r)$ and the coordination number $n_j(r)$ of j (either oxygen or hydrogen) around the paramagnetic ion. The radial distribution function was calculate as [28,29]

$$g_j(r) = \frac{\langle \rho_j(r) \rangle}{N_j/V}, \tag{1}$$

where $\langle \rho_j(r) \rangle$ is the average density of particles j at a distance r from Gd^{3+}, N_j is the total number of particles j in the simulation, and V is the volume of the simulation box. From Equation (1), we get the coordination number [28,29]

$$n_j(r) = \int_0^r 4\pi r^2 g_j(r) dr. \tag{2}$$

The dynamics of the $Gd^{3+}-$aqua complex was characterized by determining the residence time of water molecules in the inner-shell and the self-diffusivity of the complex at different temperatures. As in our earlier study, we use an indicator function to track how long the identity of water molecules in the inner shell is maintained. (The resolution is of course limited to the frequency at which we save the data.) In effect we monitor the time for the inner-shell population to rejuvenate. The dynamics of the outer-shell is described by the self-diffusion coefficient D_i

obtained through Einstein's relation [29,30]

$$D_i = \lim_{t\to\infty} \frac{1}{6t}\left[\langle \Delta r_i^2(t)\rangle\right], \quad (3)$$

where t is time, and $\langle \Delta r_i^2(t)\rangle$ is the so-called mean square displacement of particle i. Because finite-size effects of the simulation box are known to play a role in the calculation of mass-transport properties, we followed the analytical correction by Yeh and Hummer to obtain the self-diffusivity D_i^∞ at the thermodynamic limit as [31]

$$D_i^\infty = D_i + \frac{k_B T}{6\pi\eta}\frac{\xi}{L}, \quad (4)$$

where k_B is the Boltzmann constant, T is temperature, η is the shear viscosity of the system, $\xi = 2.837297$ for cubic simulation boxes [32], and L is length of the box.

2.3 ^{1}H NMR relaxivity

For N_S electron dipoles (with spin S) interacting with ^{1}H nuclear dipoles (with spin $I = 1/2$) in water, the dipole-dipole relaxation autocorrelation function $G_i^m(t)$ due to fluctuating magnetic fields around the i-th ^{1}H in water is given by [15,33,34]

$$G_i^m(t) = \frac{4\pi}{5}\left(\frac{\mu_0}{4\pi}\right)^2 \hbar^2\gamma_I^2\gamma_S^2 S(S+1) \times \frac{1}{N_S}\sum_{s=1}^{N_S}\left\langle \frac{Y_2^m\left(\Omega_{is}(t+t')\right)}{r_{is}^3(t+t')}\frac{Y_2^m\left(\Omega_{is}(t')\right)}{r_{is}^3(t')}\right\rangle_{t'}, \quad (5)$$

where t' is the lag-time, $\Omega_{is} = (\theta_{is}, \phi_{is})$ where θ_{is} is the polar angle between the dipoles and ϕ_{is} is the azimuthal angle with respect to the external magnetic field, and, Y_2^m is the spherical harmonic function. In our simulations, we usually simulate a single paramagnetic ion in the simulation box ($N_S = 1$), with a few exceptions where two paramagnetic ions are included ($N_S = 2$). Assuming an isotropic system, the dipole-dipole relaxation autocorrelation function $G_i^m(t)$ becomes independent of the order m, which is equivalent to saying that the direction of the applied static magnetic field B_0 is arbitrary. Thus assuming the case of $m = 0$ for simplicity, $Y_2^0 = \sqrt{5/16\pi}(3\cos^2\theta - 1)$ and we can rewrite Equation (5) as

$$G_i(t) = \frac{1}{4}\left(\frac{\mu_0}{4\pi}\right)^2 \hbar^2\gamma_I^2\gamma_S^2 S(S+1) \times \frac{1}{N_S}\sum_{s=1}^{N_S}\left\langle \frac{\left(3\cos^2\theta_{is}(t+t') - 1\right)}{r_{is}^3(t+t')}\frac{\left(3\cos^2\theta_{is}(t') - 1\right)}{r_{is}^3(t')}\right\rangle_{t'}, \quad (6)$$

which allows us to calculate $G_i(t)$ from MD simulation with just atomic trajectories and arbitrary directions for the magnetic field. We have calculated these autocorrelations over 7 different (and equidistant) directions for the magnetic field B_0, and we also performed a total of three independent simulations. Hence, a total of 21 autocorrelation functions were determined and averaged to the final NMR relaxation autocorrelation function.

Given that dipoles in the liquid undergo several different motions over a wide range of timescales (bond and angle stretching, rotation, translation, diffusion, etc), we can think of such processes as different frequencies of molecular motion. Because of quantum selection rules, NMR relaxation times will inherently depend on multiples (0, 1, and 2) of such frequencies in the spectral density function $J_i(\omega)$. In our simulations, given that we sample a continuous spectrum of molecular motion frequencies, we are able to recover the entire $J_i(\omega)$. This spectral density function can be calculated through the (two-sided even) Fourier transform of $G_i(t)$. i.e., [34]

$$J_i(\omega) = 2\int_0^\infty G_i(t)\cos(\omega t)dt. \quad (7)$$

where $J_i(\omega)$ is the spectral density function for the i-th ^{1}H in water.

For the case of ^{1}H ($I = 1/2$ and Larmor frequency $\omega_0 = \gamma_I B_0 = 2\pi f_0$) in water interacting with the paramagnetic ion Gd^{3+} ($S = 7/2$ and Larmor frequency $\omega_e = 658\omega_0$) implies that $\omega_e \gg \omega_0$, which yields [15]

$$\frac{1}{T_{1i}} = J_i(\omega_0) + \frac{7}{3}J_i(\omega_e). \quad (8)$$

where T_{1i} is the longitudinal relaxation time for the i-th ^{1}H in water. The total correlation function $G(t)$, total spectral density $J(\omega)$, average (i.e., observed) T_1 over the N_I ^{1}H nuclei in water are given by

$$G(t) = \sum_{i=1}^{N_I} G_i(t), \quad (9)$$

$$J(\omega) = \sum_{i=1}^{N_I} J_i(\omega), \quad (10)$$

$$\frac{1}{T_1} = \frac{1}{N_I}\sum_{i=1}^{N_I}\frac{1}{T_{1i}}, \quad (11)$$

It is more convenient to express the relaxation in terms of relaxivity r_1 as such

$$r_1 = \frac{1}{[H]}\sum_{i=1}^{N_I}\frac{1}{T_{1i}}, \quad (12)$$

where [H] = 2 [W] is the molar concentration of ^{1}H in water, and [W] $\approx$ 55,500 mM is the molar concentration of water. Note that the "fast-exchange" regime is used (i.e., r_1 is independent of residence time τ_m), which is justified in Ref. [15]. r_1 can be compared with measurements of the observed relaxation rate R_1 as such

$$R_1 = [\mathrm{Gd}]\, r_1 + R_{1,DI}, \quad (13)$$

where [Gd] is the molar concentration of gadolinium ions, and $R_{1,DI}$ is the relaxation rate of DI (de-ionized) water without paramagnetics ([Gd] = 0). For simulations where a single Gd^{3+} ion is present in a box with 2006 water molecules and PBC, the relaxivity is probed at the infinite dilution limit (details in Section 3.4).

2.4 Expansion of $G(t)$ in terms of molecular modes

In practice, because the NMR relaxation autocorrelation function obtained from simulations may not decay to zero within the simulation time span, it can be useful to decompose the signal and extract the important frequencies or modes of relaxation to be able to reconstruct the signal for longer times. Further, by decomposing the autocorrelation function into such modes of relaxation,

we can glean molecular insights into the physics of relaxation.

One key point in our approach is that dipole-dipole relaxation is assumed to have a multi-exponential decay rather than a mono-exponential decay as in the BPP and SBM models. Thus, we define

$$G(t) = \int_0^\infty P(\tau) \exp\left(-\frac{t}{\tau}\right) d\tau, \tag{14}$$

where $P(\tau)$ is the underlying distribution over correlation times τ. In this approach, the average correlation time $\langle\tau\rangle$ is given by

$$\langle\tau\rangle = \frac{1}{G(0)} \int_0^\infty P(\tau)\tau d\tau, \tag{15}$$

and the spectral density function $J(\omega)$ is determined through the Fourier transform

$$J(\omega) = \int_0^\infty \frac{2\tau}{1+(\omega\tau)^2} P(\tau) d\tau. \tag{16}$$

Finally, having the spectral density function of the system, we can obtain the spin-lattice NMR relaxation times with help of Equations (8) and (11), and also the longitudinal NMR relaxivity r_1 through Equation (12).

Observe that Equation (14) is a Fredholm integral equation of the first kind for $P(\tau)$. It is well-known that inverting Eq. (14) to obtain $P(\tau)$ is an ill-posed problem[35], especially with noisy data. To this end, we recast the problem as a minimization problem

$$\mathbf{P} = \underset{\mathbf{P}\geq 0}{\operatorname{argmin}} ||\mathbf{G} - K\mathbf{P}||^2 + \alpha||\mathbf{P}||^2, \tag{17}$$

where $\mathbf{G}$ is a column vector representing the autocorrelation function $G(t)$, $\mathbf{P}$ is a column vector that represents the distribution function $P(\tau)$, K is a kernel matrix with $K_{ij} = \exp(-t_i/\tau_j)$, and α is the regularization parameter. The above procedure is Tikhonov regularization of the original problem. We use a logarithmically spaced discretization for τ, usually with $\tau > 0.05$ ps. By setting up appropriate values of the regularization parameter α that stabilizes the solution (usually, $\alpha = 10^{-1}$), one can reconstruct the $P(\tau)$ distribution using Equation (17). These calculations are performed using an in-house code.

2.5 Experimental details

Gadolinium (III) chloride hexahydrate [$GdCl_3{\cdot}(H_2O)_6$] was purchased from Sigma Aldrich at 99% purity and used as received. Different concentrations of $GdCl_3{\cdot}(H_2O)_6$ in de-ionized water were prepared, specifically [Gd] = 0.3, 1.0 and 2.0 mM, as well as [Gd] = 0 to determine $R_{1,DI}$ for pure de-ionized water.

The ^{1}H longitudinal relaxation rate R_1 dispersions for different concentrations of the Gd^{3+}−aqua complex were measured from 30 kHz to 35 MHz (^{1}H Larmor frequency) using a Spinmaster FFC2000 1T Relaxometer (Stelar s.r.l., Mede (PV), Italy). The relaxation rate R_1 was determined using the standard pre-polarized (PP) and nonpolarized (NP) sequences[36,37]. The polarization and acquisition magnetic fields kept constant values of 15 MHz and 16.3 MHz respectively, for all experiments. The field slew rate was 13 MHz/ms and the switching time was 3 ms. Additionally, R_1 was measured at three fixed magnetic fields, namely, 90 MHz, using a permanent magnet with a magnetic field of 2.1 T; 300 MHz, performed with a NMR Varian spectrometer operating at a magnetic field of 7.0 T; and 400 MHz, performed with a Bruker spectrometer operating at a magnetic field of 9.4 T. Relaxation profiles were measured at 25 and 37°C, and experimental uncertainties were typically less than 6%, which are covered by the size of the data points in graphs.

3 Results and discussions

3.1 Structure and dynamics of inner and outer-shells

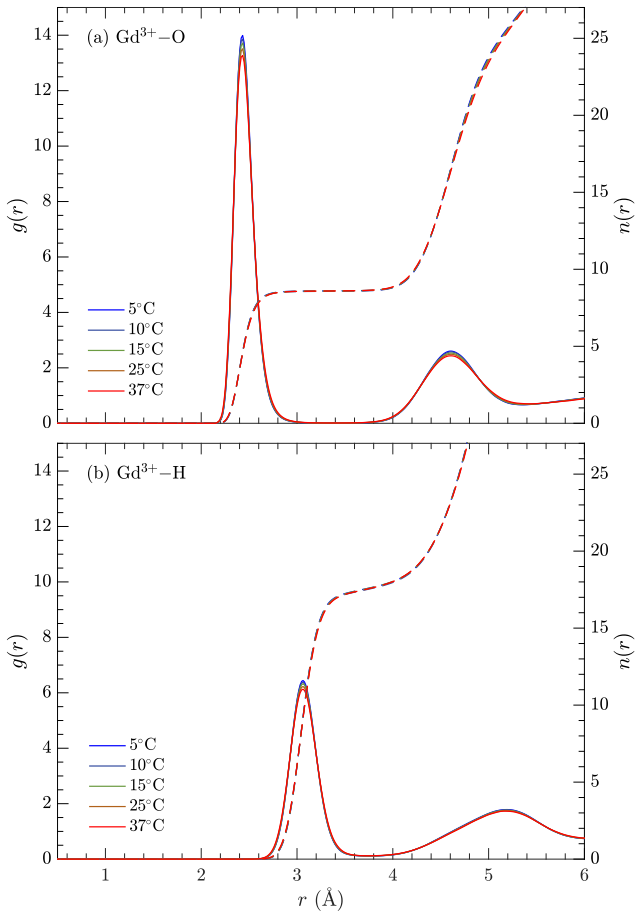

Fig. 1 Radial distribution function $g(r)$ and coordination number $n(r)$ of (a) Gd^{3+}−O and (b) Gd^{3+}−H at different temperatures. The continuous line (—) represents $g(r)$ and the dashed line (−−) represents $n(r)$.

We initially investigated the structure of the Gd^{3+}−aqua complex at different temperatures through MD simulations. From Figures 1(a) and 1(b), we observe that water molecules are highly structured around the Gd^{3+} ion due to strong electrostatic interactions between the partially negative oxygen of water and the tri-cation. These water molecules encompass the so-called inner-shell, and the coordination number of water molecules around Gd^{3+} did not change over the evaluated temperature range. We observed a coordination number around 8.5, which indicates an equal distribution of $Gd[(H_2O)_8]^{3+}$ and $Gd[(H_2O)_9]^{3+}$. The first shell of oxygen atoms around the Gd^{3+} ion is observed at r_O = 2.43 Å, while for hydrogen atoms we obtained r_H = 3.06 Å. These results are consistent with experimental data and first principle calculations in the literature, reporting about $r_O \approx 2.37 \leftrightarrow 2.5$ Å

and $r_H \approx 3.04 \leftrightarrow 3.1$ Å[8,38,39]. Overall, we observed that the structure of the inner-shell of Gd^{3+}−aqua remains approximately constant across temperatures up to human body temperature (37°C).

In contrast, the residence time analysis of water molecules immediately around the ion shows that the dynamics of the inner-shell changes considerably with temperature. Within fluctuations, the maximum residence time of water molecules in the inner-shell spans $\tau_m \simeq 1.1$ ns at 37°C to $\tau_m \simeq 1.6$ ns at 5°C. At 25°C, our estimate of $\tau_m \simeq 1.3$ ns presents good agreement with experimental and simulation data in the literature, which points to a residence time of about $\tau_m \simeq 1 \leftrightarrow 1.5$ ns[15,40]. Observe from the residence time histogram in Figure 2 that higher temperatures display the largest number of water molecules with short residence time, while lower temperatures lead to longer residence times.

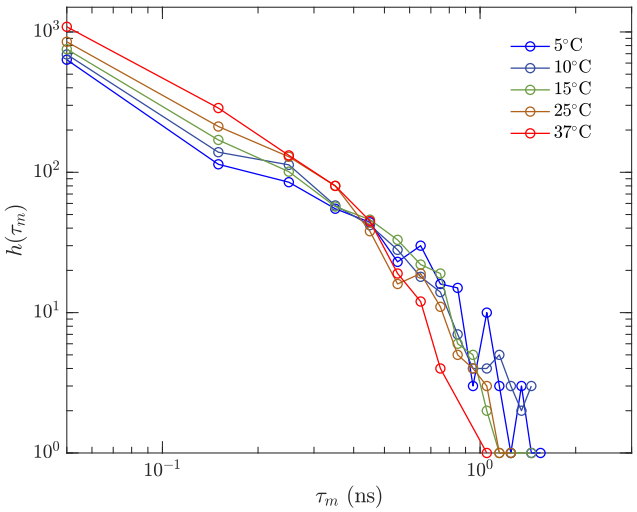

Fig. 2 Population number $h(\tau_m)$ as a function of the residence time τ of the water molecules in the inner-shell of the Gd^{3+}−aqua complex.

Figures 3(a) and 3(b) show that temperature also affects the self-diffusion of both water (D_W) and gadolinium (D_{Gd}) in the Gd^{3+}−aqua system, respectively. Hence, the outer-shell contribution to the NMR relaxation should also be impacted by thermal effects. D_W obtained with the simulations at 25°C are within 10% of measurements in pure water[41,42] and Gd^{3+}−aqua solutions (see Supplementary Information). The self-diffusion coefficients of water were corrected from finite-size effects of the simulation box using Equation (4) and the experimental viscosity values for pure water from the NIST database[43]. In the absence of available data, here we assume that the pure water viscosity is applicable for the 28 mM Gd^{3+}−aqua solution; this approximation is one possible source for the 10% deviation with measurements. Note that for pure water, our calculated D_w using NIST viscosity is in good agreement with measurements[15]. Similar corrections were not attempted for Gd^{3+} diffusion given our expectation that hydrodynamic effects will be negligible for a single solute in a fairly large simulation box. Tables S1 and S2 in the Supplementary Information presents the average box volumes and dimensions at each temperature obtained from NPT simulations, as well as the relevant viscosity values from the NIST database.

Overall, the residence time analysis suggests that whereas the

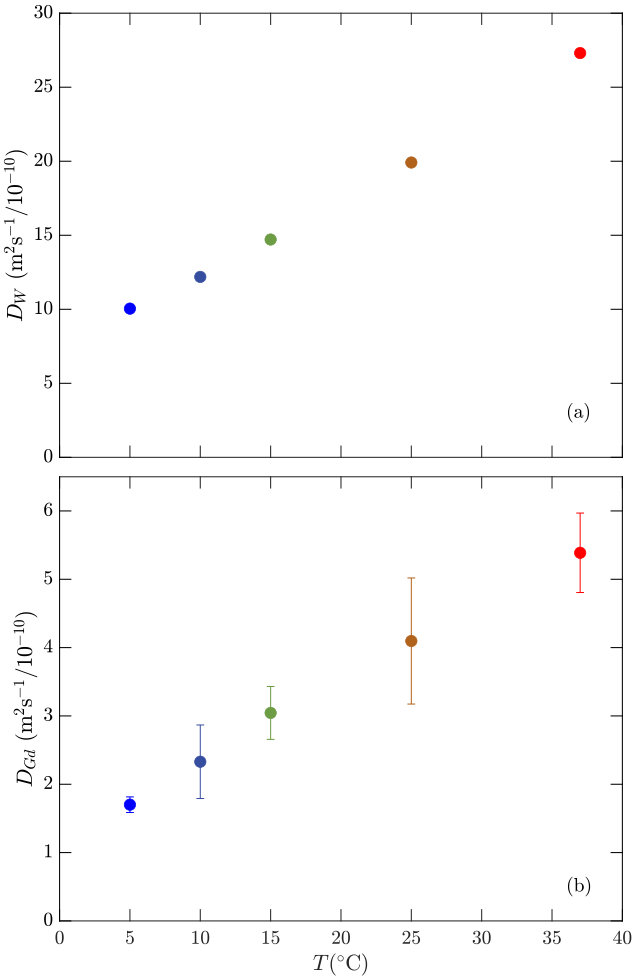

Fig. 3 Self-diffusion coefficients of both (a) water D_W and (b) gadolinium D_{Gd} in the Gd^{3+}−aqua system at different temperatures. Finite-size corrections were applied to the self-diffusion coefficient D_W of water, while the solute self-diffusivity did not need correction since hydrodynamic interactions between the solute and its periodic images are negligible.

structure of the inner-shell is not greatly affected by the increment in temperature, its dynamics and hence the NMR relaxation response of the aqua complex are susceptible to thermal effects. Also, the fact that self-diffusion coefficients are also sensitive to temperature indicates that the outer-shell contribution to the NMR relaxation is also be susceptible to thermal effects.

3.2 $^1H-Gd^{3+}$ NMR dipole-dipole autocorrelation

Figure 4(a) presents the normalized $^1H-Gd^{3+}$ NMR dipole-dipole autocorrelation function $G(t)/G(0)$ over the normalized time $t/\langle\tau\rangle$, where $\langle\tau\rangle$ is the average correlation time determine from Equation 15 and $P(\tau)$ in Figure 5. Observe that all curves collapse at short times, but diverge at longer times due to fluctuations in the autocorrelation functions. Importantly, as found earlier[15], none of the curves follow the mono-exponential decay predicted by the SBM model. This finding of the failure of the SBM model across temperatures, including temperatures of revelance for MRI imaging in humans, is an important contribution of this work.

Figure 4(b) shows the non-normalized NMR dipole-dipole au-

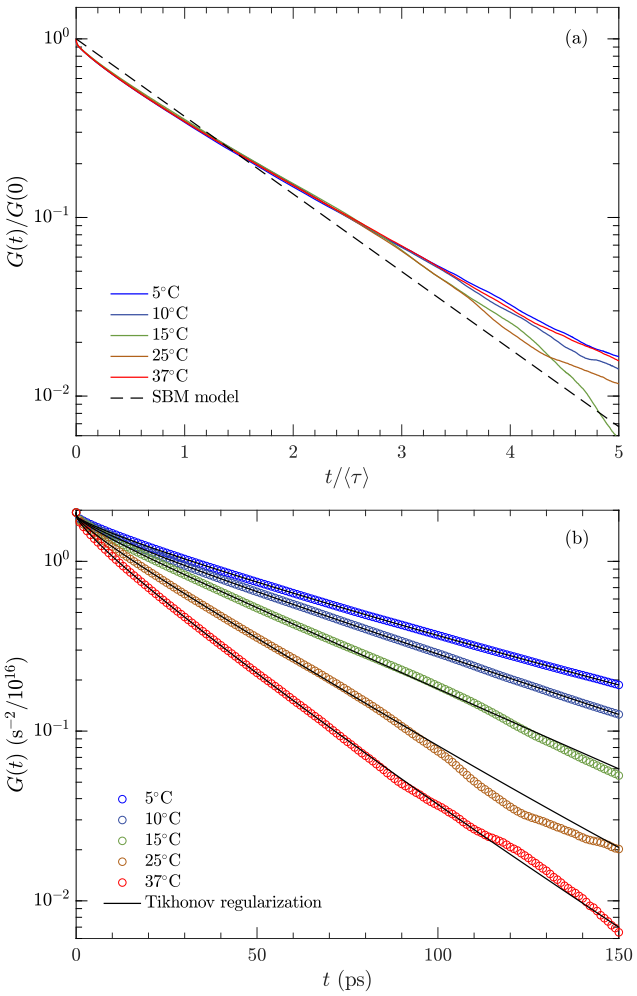

Fig. 4 NMR dipole-dipole autocorrelation function (ACF) of Gd^{3+}−aqua at different temperatures. On plot (a) we present the normalized ACF versus normalized time, and the dashed line (−−) shows a the comparison with the traditional SBM model (i.e., mono-exponential decay). On plot (b) we present the non-normalized ACF, and the continuous line (—) shows the corresponding reconstructed ACFs based on the Tikhonov regularization at different temperatures.

tocorrelation function $G(t)$ over time for Gd^{3+}−aqua at different temperatures. Observe that the absolute dipole-dipole autocorrelation function is indeed sensitive to the temperature over the studied range. 4(b) also shows the reconstructed $G(t)$ at different temperatures based on the Tikhonov regularization (Equation (17)), which agree well with with the data despite the inherent fluctuations in the original autocorrelation function at longer times.

3.3 NMR modes of relaxation

Figure 5 presents the underlying distribution $P(\tau)$ from the Tikhonov regularization, which provides insightful information about the molecular modes of NMR relaxation of the Gd^{3+}−aqua complex at different temperatures. We identify two modes, mode #1 which makes up ≃85% of $P(\tau)$, and mode #2 which makes up the remaining ≃15% of $P(\tau)$. The correlation times τ for mode #1 shorten as the temperature increases, which is quantified by a

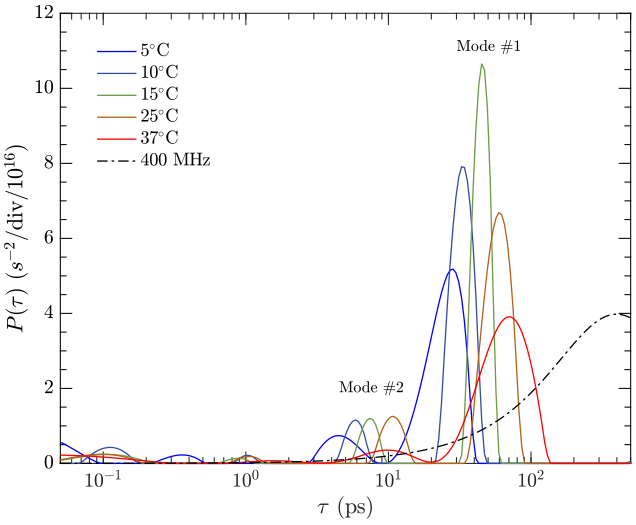

Fig. 5 Underlying distribution $P(\tau)$ of molecular modes of the NMR dipole-dipole autocorrelation functions $G(t)$ at different temperatures, obtained with the Tikhonov regularization. The two most prominent modes (#1 and #2) are identified. The dashed line (−−) shows a T_1−filter that represents the weighting of each mode of relaxation at 400 MHz, according to Equation (16)

thermal activation energy in Section 3.5. Moreover, there is a narrowing of mode #1 over the evaluated temperature range, with a maximum around 15°C; this suggests that there is a variation in activation energies within mode #1 (see Supplementary Information). The correlation times τ for mode #2 also shorten as the temperature increases, albeit with a lower thermal activation energy than mode #1, see Section 3.5.

These findings bring new fundamental physical insights into the NMR relaxation of such paramagnetic complex at a molecular scale. Ongoing investigations are being carried out to more fully explore the exact physical mechanisms behind each molecular mode in NMR relaxation, and whether or not these two modes are related to inner-shell vs outer-shell relaxation and/or conformational modes of relaxation.

3.4 ^{1}H NMR relaxivity

The ^{1}H NMR relaxivity r_1 obtained with MD simulations at different temperatures is presented in Figure 6. The longitudinal relaxivity was calculated using Tikhonov regularization with the underlying distributions $P(\tau)$ through Equation (16). It is worth noting that the NMR relaxivities r_1 obtained from the raw simulation data through FFT as in Equation (7) are significantly close to the results obtained with the Tikhonov procedure (see Figure S1 in the Supplementary Information), which supports the validity of the Tikhonov regularization. As anticipated, the fact that the dynamics of the inner and outer-shell changes with temperature greatly affects the spin-lattice relaxivity. As temperature increases and thermal fluctuations start to play a role, the capability of the Gd^{3+} ion to shorten the relaxation time T_1 of ^{1}H of water decreases, and hence NMR relaxivity r_1 decreases with temperature. The error bars were estimated using 500 bootstrap[44] samples of 7 data sets, sampled from 21 independent autocorre-

lation functions. It is important to highlight that the statistical variance without bootstrapping is about the same as the bootstrapped estimates, indicating that the bootstrapping did not artificially suppress the error as happens if the original samples are not independent.

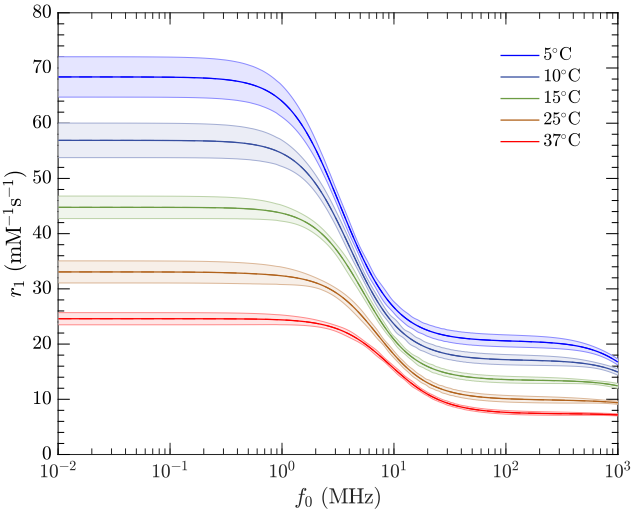

Fig. 6 NMR relaxivity r_1 obtained with MD simulations for the Gd^{3+}−aqua complex at different temperatures.

Figures 7(a) and 7(b) compare the simulation data with measurements at 25 and 37°C, respectively, where the measured relaxivity r_1 was determined using Equation 13. The measurements indicate no systematic dependence of r_1 on concentration at either at 25 or 37°C, which justifies the dilute limit[11,13] for [Gd] $\leq$ 2.0 mM.

Overall, at frequencies $f_0 \geq 5$ MHz, the simulation results agree well with measurements, especially considering the scattering of the experimental data and the simulation error bars. This points out the robustness of the MD simulations to accurately predict NMR relaxation of paramagnetic species without assuming any relaxation models or free-parameters at frequencies of interest to MRI and at different temperatures, with highlight to human body temperature (37°C). However, at frequencies $f_0 \leq 5$ MHz (not typically of interest to clinical MRI applications), the computational data do not agree with measurements because the MD simulations do not account for electron-spin relaxation, which play an important role at such lower frequencies. In fact, because of that, we can compare the relaxivity gap at low frequencies between our simulations and experiments to estimate the electron-spin relaxation contribution (see Section 3.5).

Further investigations on the effect of the counter-ion Cl^- on the spin-lattice relaxivity at low concentrations were carried out. Observe from Figure S1 in the Supplementary Information that a system with 1 Gd^{3+} / 3 Cl^- / 2006 H_2O still gives the same NMR relaxivity r_1 as the original system without the counter-ions (within error bars). This indicates that, because of the high dilution of the system, the Gd^{3+}−Cl^- interactions are small and do not greatly affect the Gd^{3+}−H relaxivity. Further, the MD simulations of a single Gd^{3+} ion are in a box with a large number of water molecules (2006 molecules), and finite system artifacts

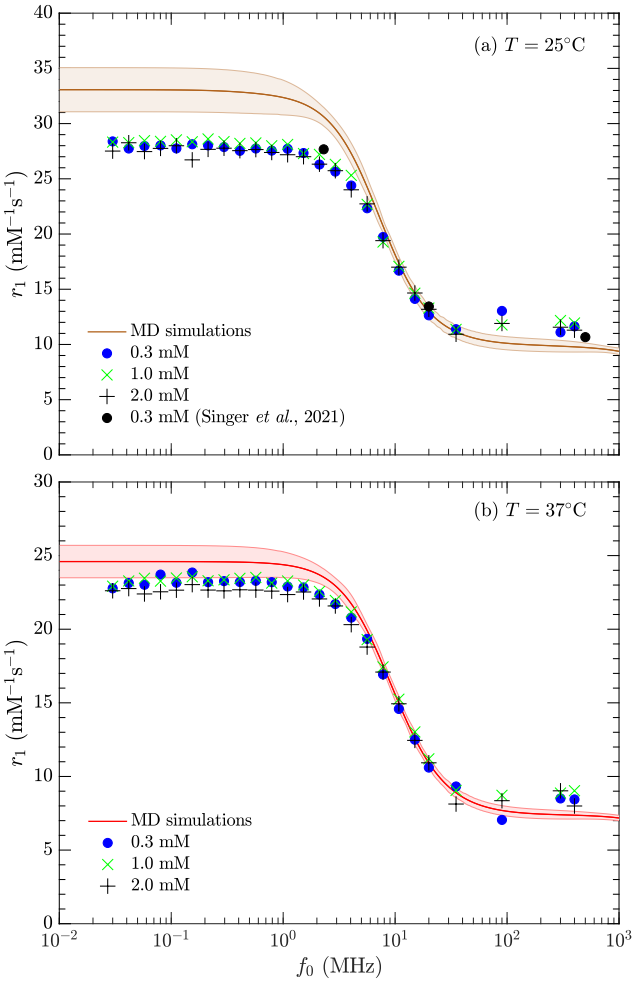

Fig. 7 Comparison of the NMR relaxivity r_1 of the Gd^{3+}−aqua complex obtained with (—) MD simulation data and experiments at concentrations of (•) 0.3 mM, (×) 1.0 mM, and (+) 2.0 mM, for both (a) 25°C and (b) 37°C.

are expected to be negligible; in effect, we simulate Gd^{3+} at infinite dilution. More generally, we can state that the nominal concentration of the simulation box is irrelevant for the calculation of NMR relaxivity r_1 provided that Gd^{3+}−Gd^{3+} interactions are negligible. Observe from Figure S2 in the Supplementary Information that within error bars the same NMR relaxivity is obtained from systems comprising 1 Gd^{3+}/3 Cl^-/1003 H_2O and 2 Gd^{3+}/6 Cl^-/2006 H_2O. Even for the smallest tested system (1003 water molecules), the periodicity artifacts are negligible. Thus, in effect, we probe the infinite dilution limit regardless of the nominal concentration of the simulation box.

Interestingly, since Gd^{3+}−Gd^{3+} interactions are negligible, we can use the infinite dilution simulated data to predict (from Equation (13)) the NMR relaxivity r_1 at different concentrations [Gd]. Figures 8(a) and 8(b) show how the projected R_1 results at different concentrations compare with measurements at 25°C and 37°C, respectively. Note that the simulated R_1 in Equation (13) are determined using the simulated r_1 together with the measured $R_{1,DI}$. While the ^{1}H-^{1}H dipole-dipole contribution to $R_{1,DI}$ has been successfully simulated before[34], the contribution from

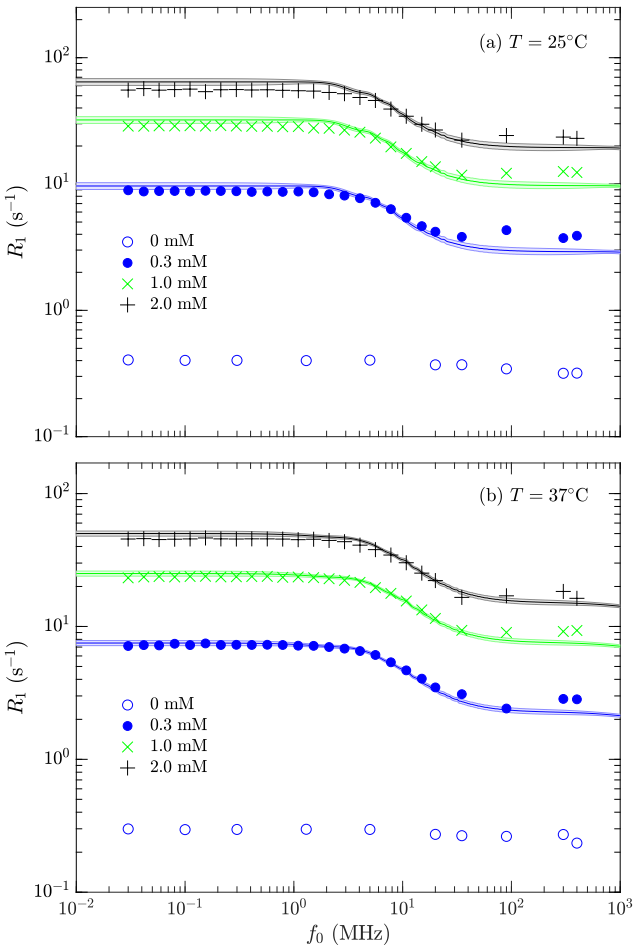

Fig. 8 Comparison of the NMR relaxivity R_1 of Gd^{3+}−aqua complex obtained with (—) extrapolated MD simulations and experiments with (○) deionized water and concentrations of Gd^{3+} ions of (•) 0.3 mM, (×) 1.0 mM, and (+) 2.0 mM, for both (a) 25°C and (b) 37°C.

paramagnetic O_2 in solution has not been attempted.

Observe from Figure 8(b) that at human body temperature the extrapolated NMR relaxivity R_1 results from MD simulations still agrees with the most concentrated experimental measurements ([Gd]= 2 mM). This indicates that simulations can still accurately predict the NMR relaxivity at frequencies $f_0 \geq 5$ MHz at human body temperature and at concentrations of paramagnetic ions much higher than the ones used in clinical MRI, which varies about 0.07 ↔ 1.0 mM[45,46].

3.5 Characteristic times and activation energies

In this section, we present a discussion on the MD simulation data in terms of activation energies. Table 1 summarizes the dynamic constants obtained with MD simulations for the maximum residence time in the inner-shell τ_m, the average correlation time $\langle\tau\rangle$, the translational-diffusion correlation time τ_D, and low-field electron-spin relaxation time T_{e0} at different temperatures. Note that τ_m (Figure 2), $\langle\tau\rangle$ (Equation (15)), τ_D (Equation (22)) and T_{e0} (Equation (25)) were determined from MD simulation data without any NMR relaxation models or free-parameters. The only assumption in determining T_{e0} is that rotational and translational-diffusion are uncorrelated with electron-spin relaxation[47].

Table 1 MD results for the maximum residence time in the inner-shell τ_m, the average correlation time $\langle\tau\rangle$, the translational-diffusion correlation time τ_D, and electron-spin relaxation time at zero frequency T_{e0}, at different temperatures. These quantities were calculated without assuming any NMR relaxation models or free-parameters.

T (°C)	τ_m (ns)	$\langle\tau\rangle$ (ps)	τ_D (ps)	T_{e0} (ps)
5	1.6	58.8	180.2	66.1
10	1.5	48.9	145.8	
15	1.5	38.5	119.2	94.6
25	1.3	28.4	88.1	152.4
37	1.1	21.2	64.7	277.6

Observe that, as temperature increases, thermal energy shortens the correlation times for rotational and translational diffusion. By assuming that thermal effects follow an Arrhenius-like increment[38,48,49], i.e.,

$$\langle\tau\rangle = \langle\tau\rangle^{\infty} \exp\left(\frac{E_A}{RT}\right), \tag{18}$$

we determine the activation energy barrier E_A for rotational and translational diffusion in the Gd^{3+}-^{1}H dipole-dipole relaxation process. We obtain the average activation energy $E_A = 23.0$ kJ.mol^{-1}, which agrees with estimates for rotational-diffusion $E_R \approx 15 \leftrightarrow 22$ kJ.mol^{-1} using measurements and the extended SBM model[38,39,48–50], as shown in Table 2.

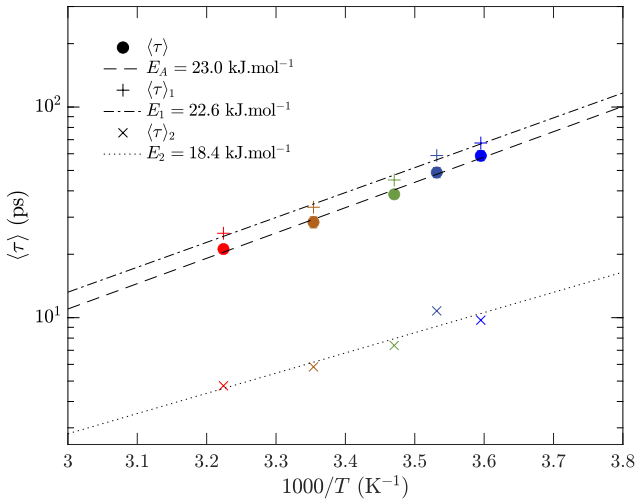

Fig. 9 Average correlation time $\langle\tau\rangle$ obtained through MD simulations at different temperatures, where the dashed line (−−) represents the fit to Equation (18) and resulting activation energy. Also shown are the equivalent quantities for the separate modes #1 and #2.

As shown in Figure 5, we can also identify mode #1 which makes up ≃85% of $P(\tau)$, and mode #2 which makes up the remaining ≃15% of $P(\tau)$. By using an appropriate cutoff τ_c at each temperature, we determine the mean correlation times $\langle\tau\rangle_{1,2}$ for modes #1 and #2 separately as such

$$\langle\tau\rangle_1 = \frac{1}{G_1(0)} \int_{\tau_c}^{\infty} P(\tau)\tau d\tau, \tag{19}$$

$$\langle\tau\rangle_2 = \frac{1}{G_2(0)}\int_{2\,\mathrm{ps}}^{\tau_c} P(\tau)\tau d\tau, \tag{20}$$

which are plotted in Figure 9. Note that we do not include the smaller peaks τ <2 ps in mode #2. Furthermore, we can determine the separate activation energies $E_{1,2}$ for each mode as such:

$$\langle\tau\rangle_{1,2} = \langle\tau\rangle_{1,2}^{\infty}\exp\left(\frac{E_{1,2}}{RT}\right), \tag{21}$$

The activation energy for mode #1 with $E_1 = 22.6$ kJ.mol^{-1} is similar to the average $E_A = 23.0$ kJ.mol^{-1}, while the activation energy for mode #2 with $E_2 = 18.3$ kJ.mol^{-1} is significantly lower. We note strong correlation coefficients R^2 = 0.992, 0.989, 0.909 between the variables $\log(\tau)$ vs $1/T$ for average, mode #1, mode #2 (respectively), which supports the use of an Arrhenius-like function.

The Supplementary Information presents the thermal activation energy E_f determined at different frequencies f_0 [51], which supports the finding in Fig. 9 that the different molecular modes have different activation energies. Ongoing simulations are being carried out to isolate the inner-shell contribution to the total NMR relaxation, and thereby determine whether modes #1 and #2 are associated with inner-shell vs outer-shell relaxation and/or conformational modes of relaxation.

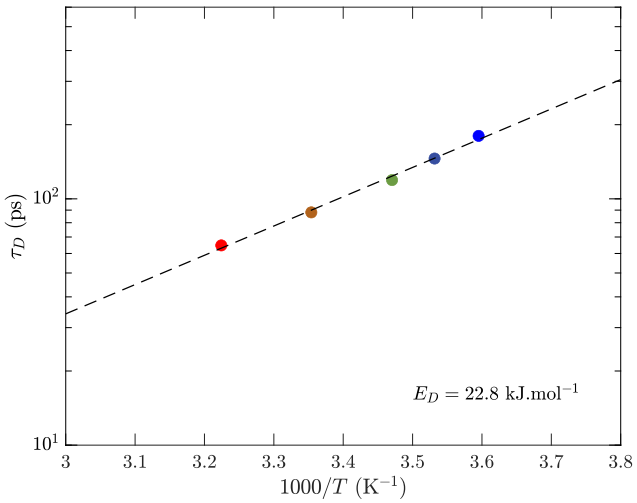

Fig. 10 Translational-diffusion correlation time τ_D obtained through MD simulations at different temperatures. The dashed line (−−) represents the fit of the data according to Equation (23).

The translational-diffusion correlation time is defined as the average time necessary for a molecule to diffuse through a diameter d_O, corresponding to the distance between the center of the paramagnetic ion and the second layer of oxygen atoms around it. τ_D can be estimated through the self-diffusivities D_W and D_{Gd} in Gd^{3+}−aqua as

$$\tau_D = \frac{d_O^2}{D_W + D_{\mathrm{Gd}}}. \tag{22}$$

In our calculations, $d_O = 4.60$ Å was determined from the radial distribution function (Figure 1(a)) and identified as constant across all studied temperatures.

Figure 10 shows how thermal effects play a role on the translational-diffusion correlation time calculated from Equation (22), showing that it shortens as temperature increase and the thermal energy increment speeds up diffusion. Again, by assuming that thermal effects on the translational-diffusion relaxation also follow an Arrhenius-like decay, we state that

$$\tau_D = \tau_D^{\infty}\exp\left(\frac{E_D}{RT}\right), \tag{23}$$

from where we can similarly estimate the activation energy barrier E_D of the translation-diffusion contribution to the relaxation. We obtain that $E_D = 22.8$ kJ.mol^{-1}, in good agreement with estimates in the literature of about ~ 22 kJ.mol^{-1} [38,49], which were obtained from multi-parameter fits of NMR/EPR experimental relaxation data assuming the outer-shell HF model within the extended SBM model. Table 2 summarizes these comparisons, which according to simulations indicates that E_D is consistent with E_A.

One can qualitatively assess whether the outer-shell contribution to r_1 exists by comparing the value of τ_D to the distribution in molecular modes $P(\tau)$ in Figure 5. As explained previously [15], the Hwang-Freed model [18] indicates that a conversion factor of 9/4 be applied $\tau_D = 9/4\tau_T$, where τ_T is the proper quantity to be compared with the simulated $P(\tau)$. The diffusion data and Equation 22 predict that τ_T lies within mode #1 of $P(\tau)$ at all temperatures, which suggests that the outer-shell contribution may indeed contribute to r_1 at all temperatures. Note that this prediction assumes the Hwang-Freed model.

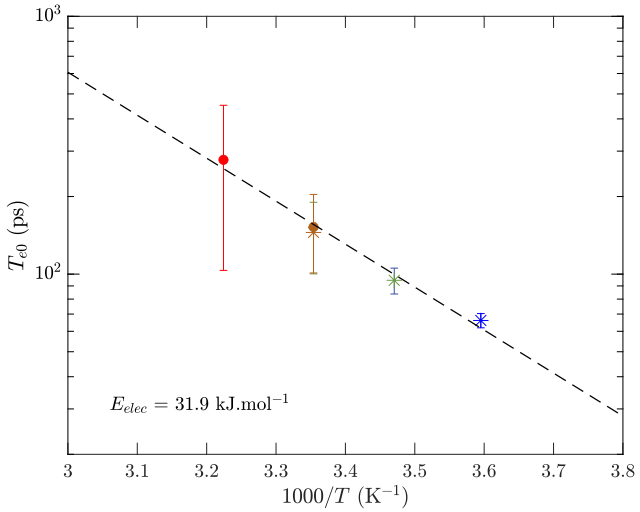

Fig. 11 Electron-spin relaxation correlation time T_{e0} obtained through the difference between MD simulations and experiments from (•) this work and (✳) Koenig *et al.*, 1975 [52]. The dashed line (−−) represents the fit of the data according to Equation (26).

Besides the rotational and translational-diffusion contributions, electron-spin relaxation also plays a role at low frequencies. The longitudinal and transverse contributions of the electron-spin relaxation are defined as T_{1e} and T_{2e}, respectively. At zero frequency ($\omega_S = 0$), a.k.a. low field, we define $T_{1e}(0) = T_{2e}(0) = T_{e0}$. By assuming that the rotational and translational-diffusion are uncorrelated with the electron-spin relaxation time T_{e0} at zero fre-

quency[47], we obtain that low-field value

$$r_1'(0) = \frac{1}{[\mathrm{H}]}\frac{20}{9}\Delta\omega^2\langle\tau'\rangle, \tag{24}$$

$$\frac{1}{\langle\tau'\rangle} = \frac{1}{\langle\tau\rangle} + \frac{1}{T_{e0}}, \tag{25}$$

where $r_1'(0)$ is the NMR relaxivity at $f_0 = 0$ MHz, and $\Delta\omega^2 = 3G(0)$ is the strength of the second-moment of the dipole-dipole interactions.

As stated in Section 3.4, the molecular force-field employed in our MD simulations does not capture the physics of electron-spin relaxation, and hence the simulation data can subtracted from experimental measurements at low frequency to isolate the contribution of electron-spin relaxation using Equations (24) and (25)[15]. Figure 11 shows the electron-spin relaxation time T_{e0} at different temperatures, from where we observe that thermal effects increases T_{e0} and thus weakens electron-spin relaxation. In fact, by analyzing Figures 7(a) and 7(b), we observe that MD results at low frequency (without the electron-spin relaxation contribution) at 37°C is closer to experimental measurements than the comparison between simulations and experiments at low frequencies for 25°C. Assuming a exponential law decay for the electron-spin relaxation time as function of temperature,

$$T_{e0} = T_{e0}^{\infty}\exp\left(-\frac{E_{elec}}{RT}\right), \tag{26}$$

we obtain that $E_{elec} = 31.9$ kJ.mol^{-1}. Table 2 compares this result to other estimates in the literature based on parameter fitting of experimental data to the BPP model. Despite the lack of agreement, it is worth noting that our result is the first-of-its-kind where molecular simulations and experiments were employed to estimate the activation energy for the electron-spin relaxation of Gd^{3+} in water at zero frequency, without any models or free parameters, except for the assumption that rotational and translational-diffusion are uncorrelated with the T_{e0}.

Table 2 MD results and experimental comparisons of thermal activation energies for rotational-diffusion (E_R), or E_A from simulations*, translational-diffusion (E_D), and electron-spin relaxation (E_{elec}).

	E_R (kJ.mol^{-1})	E_D (kJ.mol^{-1})	E_{elec} (kJ.mol^{-1})
MD simulations	23.0*	22.8	31.9
Reference[38]	15.0 ± 1.3	22.0	18.4 ± 1.4
Reference[39]	19.0	22.0	14.9 ± 2
Reference[48]	21.48 ± 0.03		0 ± 6.33
Reference[49]	18.9		9.2
Reference[50]	15.1 ± 1.5		15.4 ± 1.1

4 Conclusions

We have employed semi-classic MD simulations *without assuming any NMR relaxation models or free-parameters* to investigate thermal effects and discuss the role of concentration on the spin-lattice NMR relaxivity r_1 of the Gd^{3+}−aqua complex. Our experimental measurements validate the MD approach at clinical MRI conditions of human body temperature (37°C), concentration of the paramagnetic ions in the body (0.07 ↔ 1.0 mM)[45,46], and typical frequencies of interest in clinical MRI ($20 \le f_0 \le 130$ MHz), supporting the robustness of the MD approach. We have also estimated error bars and uncertainties in both MD simulations and measurements, which allowed a consistent statistical comparison of the data across different temperatures and concentrations.

Although simulations have shown that the structure of the inner-shell of Gd^{3+}−aqua does not appreciably change between 5 and 37°C, the dynamics of this paramagnetic complex is greatly susceptible to thermal effects. Residence time analysis show that the rejuvenation time of the inner-shell spans from about $\simeq 1.1$ ns at 37°C to $\simeq 1.6$ ns at 5°C. We find that the self-diffusivity of Gd^{3+}−aqua also changes appreciably with temperature, which affects the outer-shell relaxation.

We show that the SBM model for relaxation from rotational diffusion alone fails to predict the multi-exponential nature of the simulated autocorrelation function $G(t)$ of such paramagnetic complexes. Our approach of decomposing $G(t)$ into the underlying distribution of molecular modes $P(\tau)$ provides new insights into the distribution of molecular correlation times τ. We observe two prominent molecular modes with different thermal activation energies, indicating different physical mechanisms on the molecular scale. Further studies are required to determine whether each mode corresponds to inner versus outer shell contributions.

We find that the simulated average activation energy $E_A = 23.0$ kJ.mol^{-1} agrees with literature values E_R for rotational diffusion obtained from measurements and fits to the extended SBM model. The simulated translational-diffusion activation energy $E_D = 22.8$ kJ.mol^{-1} also agrees with literature values obtained from measurements and fits to the extended SBM model. Because the molecular models employed do not capture electron-spin relaxation effects, we employ a new approach by combining low frequency ($f_0 \le 1$ MHz) simulation results with measurements to isolate electron-spin contributions and estimate its activation energy, which is found to be $E_{elec} = 31.2$ kJ.mol^{-1}.

The current MD simulations explore the infinite dilution limit, which can also be adapted for other paramagnetic ions in which the infinite dilution is a good approximation. Having validated the MD simulation approach for prediction of NMR relaxivity at temperature, ion concentration and magnetic field frequencies of interest to MRI, the next steps of the work include further investigating the physical mechanisms of the molecular modes of relaxation in $P(\tau)$ and using our MD computational approach to study chelated GBCAs and other contrast agents of clinical interest.

Conflicts of interest

There are no conflicts to declare.

Acknowledgements

We thank the Robert A. Welch Foundation (Grant C-1241), The Ken Kennedy Institute, the Rice University Creative Venture Funds (Faculty Initiative Fund), and the Rice University Consortium on Processes in Porous Media for the financial support. We also thank Dr. George J. Hirasaki and Dr. Amanda M. Marciel for the insightful discussions and support provided to this project. We acknowl-

edge the organizers and sponsors of the training at Molecular Dynamics/Monte Carlo Summer School, organized by the Institute for Computational Molecular Science Education. We also thank Dr. Phillip Stallworth (Hunter College) for technical assistance with setting up the 90 MHz relaxation measurements.

Notes and references

1 A. E. Merbach and E. Toth, *The Chemistry of contrast agents in Medical Magnetic Resonance Imaging*, John Wiley & Sons, 1st edn, 2001.

2 S. Aime, M. Botta, D. Esteban-Gómez and C. Platas-Iglesias, *Molecular Physics*, 2019, **117**, 898–909.

3 R. Sethi, J. S. Ananta, C. Karmonik, M. Zhong, S. H. Fung, X. Liu, K. Li, M. Ferrari, L. J. Wilson and P. Decuzzi, *Contrast Media and Molecular Imaging*, 2012, **7**, 501–508.

4 M. Rogosnitzky and S. Branch, *BioMetals*, 2016, **29**, 365–376.

5 A. M. Panich, M. Salti, S. D. Goren, E. B. Yudina, A. E. Aleksenskii, A. Y. Vul and A. I. Shames, *Journal of Physical Chemistry C*, 2019, **123**, 2627–2631.

6 C. Diaferia, E. Gianolio, T. Sibillano, F. A. Mercurio, M. Leone, C. Giannini, N. Balasco, L. Vitagliano, G. Morelli and A. Accardo, *Scientific Reports*, 2017, **7**, 1–14.

7 S. Zhang, M. Merritt, D. E. Woessner, R. E. Lenkinski and A. D. Sherry, *Accounts of Chemical Research*, 2003, **36**, 783–790.

8 O. V. Yazyev and L. Helm, *Journal of Chemical Physics*, 2007, **127**, 1–8.

9 Y. D. Xiao, R. Paudel, J. Liu, C. Ma, Z. S. Zhang and S. K. Zhou, *International Journal of Molecular Medicine*, 2016, **38**, 1319–1326.

10 J. A. Pople, W. G. Schneider and H. J. Bernstein, *High Resolution Nuclear Magnetic Resonance*, McGraw-Hill Book Company, 1st edn, 1958.

11 I. Solomon, *Physical Review*, 1955, **99**, 559–565.

12 N. Bloembergen, *The Journal of Chemical Physics*, 1957, **27**, 572–573.

13 N. Bloembergen and L. O. Morgan, *The Journal of Chemical Physics*, 1961, **34**, 842–850.

14 N. Bloembergen, E. M. Purcell and R. V. Pound, *Physical Review*, 1948, **73**,.

15 P. M. Singer, A. V. Parambathu, T. J. P. D. Santos, Y. Liu, L. B. Alemany, G. J. Hirasaki, W. G. Chapman and D. Asthagiri, *Physical Chemistry and Chemical Physics*, 2021, **23**, 20974–20984.

16 P. M. Singer, A. Valiya Parambathu, X. Wang, D. Asthagiri, W. G. Chapman, G. J. Hirasaki and M. Fleury, *Journal of Physical Chemistry B*, 2020, **124**, 4222–4233.

17 A. Valiya Parambathu, P. M. Singer, G. J. Hirasaki, W. G. Chapman and D. Asthagiri, *Journal of Physical Chemistry B*, 2020, **124**, 3801–3810.

18 L. P. Hwang and J. H. Freed, *The Journal of Chemical Physics*, 1975, **63**, 4017–4025.

19 H. C. Torrey, *Physical Review*, 1953, **92**, 962–969.

20 Y. Ayant, E. Belorizky, J. Aluzon and J. Gallice, *Journal de Physique*, 1975, **36**, 991–1004.

21 R. Uzal-Varela, L. Valencia, D. Lalli, M. Maneiro, D. Esteban-Gómez, C. Platas-Iglesias, M. Botta and A. Rodríguez-Rodríguez, *Inorganic Chemistry*, 2021, **60**, 15055–15068.

22 J. Wahsner, E. M. Gale, A. Rodríguez-Rodríguez and P. Caravan, *Chem. Rev.*, 2019, **119**, 957–1057.

23 P. Ren and J. W. Ponder, *Journal of Physical Chemistry B*, 2003, **107**, 5933–5947.

24 C. Clavaguera, F. Calvo and J. P. Dognon, *Journal of Chemical Physics*, 2006, **124**, 1–8.

25 P. Eastman, J. Swails, J. D. Chodera, R. T. McGibbon, Y. Zhao, K. A. Beauchamp, L. P. Wang, A. C. Simmonett, M. P. Harrigan, C. D. Stern, R. P. Wiewiora, B. R. Brooks and V. S. Pande, *PLoS Computational Biology*, 2017, **13**, 1–17.

26 J. A. Rackers, Z. Wang, C. Lu, M. L. Laury, L. Lagardère, M. J. Schnieders, J. P. Piquemal, P. Ren and J. W. Ponder, *Journal of Chemical Theory and Computation*, 2018, **14**, 5273–5289.

27 L. Martinez, R. Andrade, E. G. Birgin and J. M. Martínez, *Journal of Computational Chemistry*, 2009, **30**, 2157–2164.

28 D. C. Rapaport, *The Art of Molecular Dynamics Simulation*, Cambridge University Press, 2nd edn, 2004.

29 D. Frenkel and B. Smit, *Understanding molecular simulation: from algorithms to applications*, Academic Press, 2nd edn, 2002.

30 A. Einstein, *Annalen der Physik*, 1905, **322**, 549–560.

31 I. C. Yeh and G. Hummer, *Journal of Physical Chemistry B*, 2004, **108**, 15873–15879.

32 H. Hasimoto, *Journal of Fluid Mechanics*, 1958, **5**, 317–328.

33 J. McConnell, *The Theory of Nuclear Magnetic Relaxation in Liquids*, Cambridge University Press, 1st edn, 2009.

34 P. M. Singer, D. Asthagiri, W. G. Chapman and G. J. Hirasaki, *Journal of Magnetic Resonance*, 2017, **277**, 15–24.

35 P. M. Singer, D. Asthagiri, Z. Chen, A. V. Parambathu, G. J. Hirasaki and W. G. Chapman, *Journal of Chemical Physics*, 2018, **148**, 1–10.

36 R. Kimmich and E. Anoardo, *Progress in Nuclear Magnetic Resonance Spectroscopy*, 2004, **44**, 257–320.

37 E. Anoardo, G. Galli and G. Ferrante, *Applied Magnetic Resonance*, 2001, **20**, 365–404.

38 D. H. Powell, O. M. N. Dhubhghaill, D. Pubanz, L. Helm, Y. S. Lebedev, W. Schlaepfer and A. E. Merbach, *Journal of the American Chemical Society*, 1996, **118**, 9333–9346.

39 A. Borel, F. Yerly, L. Helm and A. E. Merbach, *Journal of the American Chemical Society*, 2002, **124**, 2042–2048.

40 R. V. Southwood-Jones, W. L. Earl, K. E. Newman and A. E. Merbach, *Journal of Physical Chemistry*, 1980, **73**, 5909–5918.

41 R. Mills, *The Journal of Physical Chemistry*, 1973, **77**, 685–688.

42 E. O. Stejskal and J. E. Tanner, *The Journal of Chemical Physics*, 1965, **42**, 288–292.

43 P. Linstrom and W. Mallard, *NIST Chemistry WebBook*, NIST Standard Reference Database Number 69, National Institute of Standards and Technology, 2022.

44 B. Efron and R. J. Tibshirani, *An introduction to the Bootstrap*,

CRC Press, 1st edn, 1998.

45 E. Lancelot, J. Froehlich, O. Heine and P. Desché, *Acta Radiologica*, 2016, **57**, 1334–1343.

46 S. Fujita, M. Nakazawa, A. Hagiwara, R. Ueda, M. Horita, T. Maekawa, R. Irie, C. Andica, K. K. Kumamaru, M. Hori and S. Aoki, *Magnetic Resonance in Medical Sciences*, 2019, **18**, 260–264.

47 J. Kowalewski, L. Nordenskiöld, N. Benetis and P.-O. Westlund, *Prog. Nucl. Magn. Reson. Spect.*, 1985, **17**, 141–185.

48 A. Borel, Éva Tóth, L. Helm, A. Jánossy and A. E. Merbach, *Physical Chemistry Chemical Physics*, 2000, **2**, 1311–1317.

49 S. Rast, A. Borel, L. Helm, E. Belorizky, P. H. Fries and A. E. Merbach, *Journal of the American Chemical Society*, 2001, **123**, 2637–2644.

50 K. Micskei, D. H. Powell, L. Helm, E. Brücher and A. E. Merbach, *Magnetic Ressonance in Chemistry*, 1993, **31**, 1011–1020.

51 R. A. Bernheim, T. H. Brown, H. S. Gutowsky and D. E. Woessner, *The Journal of Chemical Physics*, 1959, **30**, 950–956.

52 S. H. Koenig and M. Epstein, *The Journal of Chemical Physics*, 1975, **63**, 2279–2284.